Porous nickel-alumina derived from metal-organic framework (MIL-53): a new approach to achieve active and stable catalysts in methane dry reforming

Leila Karam, Julien Reboul, Sandra Casale, Pascale Massiani, Nissrine El Hassan

Porous nickel-alumina derived from metal-organic framework (MIL-53): a new approach to achieve active and stable catalysts in methane dry reforming.

Leila Karam[a,b], Julien Reboul[a]*, Sandra Casale[a], Pascale Massiani[a], Nissrine El Hassan[b]

[a] Sorbonne Université, UPMC Université Paris 06, CNRS UMR 7197, Laboratoire de Réactivité de Surface, 4 Place Jussieu, 75005 Paris, France. Julien.reboul@upmc.fr

[b] Department of Chemical Engineering, Faculty of Engineering, University of Balamand, P.O. Box 33, Amioun, El Koura, Lebanon.

KEYWORDS. Nickel nanoparticles on alumina catalysts, dry reforming of methane, metal-organic framework

ABSTRACT: An Al-containing MIL-53 metal-organic framework with very high surface area (S_{BET} = 1130 $m^2.g^{-1}$, N_2 sorption) was used as sacrificial template to prepare a nickel-alumina-based catalyst (Ni^0Al_{MIL}) highly active and stable in the reaction of dry reforming of methane (DRM). The procedure consisted in impregnating the activated (solvent free) MIL-53 sample with a nickel precursor solution, then calcining the material to remove the organic linkers and subsequently reducing it to form the reduced nickel active phase. At the step of calcination, this procedure results in the formation of a porous uniform spinel phase with Ni nanospecies embedded in the alumina-based matrix, as deduced from XRD, TPR and TEM analyses. This leads after reduction to a porous lamellar γ-Al_2O_3 material with small Ni^0 nanoparticles homogeneously dispersed and stabilized within the support. The performances of this catalyst in DRM are better than those of two reference Ni@alumina catalysts prepared for comparison by conventional nickel impregnation of two preformed alumina supports: a first one obtained by calcination of MIL-53 (Al_{MIL}) and a second one consisting of a commercial γ-Al_2O_3 batch (Al_{COM}). The higher CH_4 and CO_2 conversions (till 3 times higher than on $Ni^0@Al_{COM}$), high catalytic stability (no loss of activity after 13-100h) and higher selectivity towards DRM (H_2:CO products ratio remaining at 1) on Ni^0Al_{MIL} compared to the other catalysts is believed to come from the particularly strong interaction between the nickel and alumina phases generated by using the unique high specific surface of the parent MOF support to deposit nickel. This creates an intimate mixing favorable to a persisting interaction of the nickel nanoparticles with the alumina support in the reduced material. The lamellar shape of the γ-Al_2O_3 composing the catalyst and its

remaining high specific surface may also contribute to the excellent Ni resistance to sintering and in turn to the inhibition of carbon nanotubes formation during the reaction.

1. Introduction

In a world where both global warming and oil resources substitution have become major environmental issues, the reaction of dry reforming of methane (DRM) is taking great attention. This reaction targets the transformation of CH_4 and CO_2, which are two abundant greenhouse gases, into a syngas with equimolar CO and H_2 composition perfectly suited for further production of hydrocarbons by Fischer-Tropsch synthesis [1–3]. In spite of many studies dedicated to the topic, DRM has not reached yet the industrial level due to the lack of active and stable catalysts being also economically viable. At present, the most effective active phases in DRM are noble metals which have the disadvantage to be rare and expensive [4–6]. Hence, developing catalysts based on cheaper and more abundant active phases is strongly desirable. Amongst the family of transition metals that represents the best alternative, nickel is the most promising one [7]. However, most of the existing catalysts using common oxide supports as well conventional nickel deposition routes face two important drawbacks: firstly metal sintering, which is accentuated by the high temperature at which the reaction has to be carried out due to thermodynamic reasons [8,9]; secondly, important formation of carbon deposits during the course of the reaction, due to the occurrence of CH_4 decomposition as side reaction [10,11] that leads to progressive activity loss by inhibiting the active sites and to plugging of the reactor when carbon nanotubes are formed in big amount [12,13]. In the last decade, numerous attempts like the use of a bimetallic catalyst [14–16] or altering the type of support [17,18] have been made to overcome these barriers and design more robust catalysts.

Recently, we showed that an efficient route to limit nickel sintering consists in using supports with high specific area and organized mesopores where the nickel nanoparticles can be occluded, leading not only to their stabilization against growing but also to their protection against carbon nanotube formation that is inhibited owing to steric constraints [19–22]. Enhancing the interaction between the nickel active phase and the support was also found to play a determining role, especially when using ordered mesoporous alumina with high specific surface as support [23,24]. Furthermore, increased interaction and performances were reached on this type of support by preparing the catalysts via a one-pot method consisting in introducing the nickel active phase directly during the synthesis of the alumina matrix instead of adding it by conventional post-synthesis impregnation treatment [25,26]. With such one-pot method combined to an Evaporation-Induced Self-Assembly (EISA) route, we recently synthesized well organized mesoporous Ni/alumina materials where nickel was integrated as isolated species in the walls. This led to a high nickel dispersion after reduction as well as after subsequent catalytic test in the harsh conditions of DRM [27], with mean size of the metal nanoparticles in the spent catalysts much below those commonly reported in the literature [28–31]. The benefits of intimately mixing the active metal and the support precursors at the steps of material synthesis was

similarly demonstrated in the literature in works where DRM catalysts were prepared via a solid-phase crystallization route consisting in first exchanging a mineral precursor (perovskites, hydrotalcites, pyrochlores or spinels) with nickel cations, then calcining it to obtain a nickel-containing oxide solid solution and finally reducing it to give the catalyst [32,33]. However, although active and stable, these last catalysts were poorly porous and had low specific surfaces, which is known to be detrimental to active site accessibility and therefore to catalytic performances.

Based on these previous studies, our purpose in the present work is to combine the advantages of high porosity, high surface area and intimate mixing between the nickel and support components to synthesize highly stable and active Ni/alumina catalysts for DRM. To this end, we chose to use an Al-containing Metal-organic framework (MOF) as sacrificial precursor to prepare the catalysts. MOFs are highly porous hybrid materials made up by the regular assembly of metal clusters connected to one another's by multifunctional organic linkers. They are characterized by extremely high specific surfaces and pore volumes that make them of great interest as host materials as was already demonstrated in many applications such as gas storage, molecular separation or sensing [34]. In the field of catalysis, the high accessibility of their metal nodes and their reactivity have started to be exploited as well, even if stability issues in the conditions of catalysis still often remain to be solved. Besides, the scope of MOF application was recently broadened by using these hybrid materials as sacrificial templates to synthesize either carbonaceous or purely inorganic materials with unique textural properties depending on the thermal treatment used for their transformation [35–38].

In this contribution, the selected MOF is an aluminum-based MIL-53(Al) composed of aluminum hydroxyl chains connected by terephthalate organic linkers and running along one-dimensional channels. It gathers the attributes required to obtain a porous nickel-alumina solid solution after its calcination: on one hand, it possesses a high porosity and metal-cluster accessibility expected to favor the homogeneous dispersion of nickel species within the oxide structure; on the other hand, it contains organics whose decomposition enables the formation of porosity in the obtained alumina [39]. An additional benefit is the occurrence in this structure of aluminum bridging hydroxy groups lying along the inorganic chains that can interact with the nickel precursors and hence act as anchorage sites. Moreover, MIL-53(Al) is made from the assembly of relatively inexpensive components, namely hydroxy-aluminum species and terephthalate linkers, which can be extracted from natural or recycled feedstocks [40,41] making this MOF-derived strategy economically and ecologically viable.

The strategy followed for material synthesis and activation is depicted in Fig. 1. After synthesis and activation (solvent removal) of the parent MIL-53(Al), a cationic nickel precursor is impregnated within the pores (step a), then calcination is performed to obtain a porous Ni/Al oxide solid solution (step b) that is finally thermally treated under H_2 to form the reduced nickel nanoparticles that constitute the active phase for DRM. At all steps of the preparation, the materials are thoroughly characterized by complementary techniques (XRD, N_2 sorption, TG/MS and TEM) to understand the evolution of both the alumina-based support (texture and structure) and the supported nickel active phase (dispersion,

location and state). In order to check the relevance of our strategy, and especially to evidence the benefit of occluding the nickel precursor within the MOF framework before its calcination, the performances of the obtained reduced catalyst are also compared to those of a nickel-alumina catalyst prepared by the impregnation of nickel within the pores of already calcined MIL-53(Al) as well as a more traditional nickel-alumina catalyst made by Ni impregnation of a commercial γ-alumina.

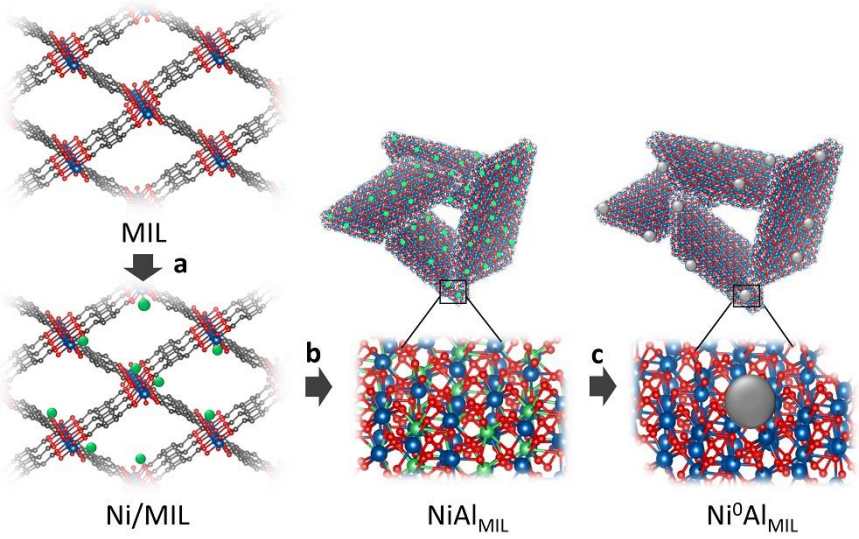

Figure 1. Schematic view of the innovative MOF-based preparation route of the Ni-alumina catalyst: (a) impregnation of the activated MIL-53(Al) with an aqueous $Ni(NO_3)_2$ solution to obtain Ni/MIL followed by (b) calcination at 500 °C to form the porous $NiAl_{MIL}$ solid solution and (c) reduction under H_2 at 800 °C to give the Ni^0Al_{MIL} catalyst. The grey color is for carbon atoms, blue is for aluminum, red for oxygen and green for nickel.

2. Experimental

2.1 Materials preparation

The parent Al-containing MIL-53(Al) material was synthesized according to a known microwave-based procedure reported to provide nanocrystallites of homogeneous distribution in shape and size [40]. It consisted in mixing 1.21 g of $AlCl_3.6H_2O$ and 0.42 g of benzene-1,4-di-carboxylic acid with 3 ml water and 5 ml of dimethylformamide (DMF), then transferring the mixture into a 50 ml reactor and heating it in a microwave oven for 30 minutes at 125 °C and with a power of 200 W. The solid was recovered by centrifugation and washed six times in 10 ml of DMF then in 10 ml of deionized water to ensure full removal of unwanted residues. After the last centrifugation, the white powder was dried for 24 h at 70 °C and heated in air at 220 °C for 72 h to remove the structuring agent and obtain the activated **MIL** sample. Nickel introduction was carried out by incipient wetness impregnation performed on the sample freshly dehydrated at 80 °C in an oven overnight. The procedure consisted in adding

dropwise a $Ni(NO_3)_2.6H_2O$ aqueous solution with a volume equal to the pore volume of the MOF support (as estimated from N_2-sorption analysis, see below) and a Ni concentration established as to correspond to a Ni/Al atomic ratio in the sample of 0.07 (i.e. final Ni content in the dry catalyst of 5 wt%). The solid obtained after drying at room temperature for 24 h is hereafter denoted **Ni/MIL**. Part of it was kept as such to perform hydration-dehydration tests (see section 3.1) and the other part was submitted to calcination in air for 5 h at 500 °C (thin bed conditions, heating rate 0.5 °C.min^{-1}) to give **$NiAl_{MIL}$**.

For comparison purposes, two reference samples were also prepared from two distinct preformed alumina supports. The first one was obtained by placing the above MIL material in a ceramic plate and heating it in static air at 500 °C (heating rate 0.5 ° C.min^{-1}) for 5 h to remove the organic linkers and lead to an alumina material (**Al_{MIL}**). The second support (**Al_{COM}**) was a conventional γ-alumina obtained by calcination at 500 °C in air of a commercial Boehmite (Sasol Plural, an alumina hydrate AlOOH). After impregnation (5 wt% Ni, same conditions as above) followed by calcination in air at 500 °C, these two alumina supports gave samples **Ni@Al_{MIL}** and **Ni@Al_{COM}**, respectively.

2.2 Physicochemical characterization techniques

Elemental compositions (Ni and Al contents) were obtained by X-fluorescence (XRF) on a XEPOS spectrometer (Spectro Ametek) using a micropowder method and a calibration curve previously established from NiO and alumina mixtures with known chemical compositions.

Powder X-Ray diffractograms (PXRD) were registered on a PANalytical X'pert Powder instrument operated at 10 mA and 30 kV, using the Cu X-ray wavelength (λ=1.5405 nm). Crystalline phases were identified by referring to the international center for diffraction data (ICDD). The Scherer equation was applied to evaluate the average size (D in nm) of crystal domains, expressed as $D=K\lambda/\beta\cos\theta$ where K=0.9 is a constant, λ is the wavelength, β is the full width at half maximum (FWHM) of the diffraction peaks, and θ corresponds to peak position.

N_2-sorption adsorption-desorption isotherms were registered on an ASAP 2020 Micromeritics apparatus at -198 °C. Prior to analysis, the materials were degassed at 120 °C for 12h. BET (Brunauer-Emmett-Teller) surface areas were calculated within the relative pressure range 0.05-0.3. Total pore volumes were determined at saturation of the N_2 sorption. Micropore volumes were determined by the t-plot method and pore diameters were determined from the BJH (Barrett-Joyner-Halenda) model by using the desorption branch.

Reducibilities of the calcined materials were determined from temperature-programmed reduction (TPR) experiments carried out on an Autochem 2920 Micromeritics apparatus. Approximately 70-100 mg of the sample deposited on quartz wool in a U-shaped quartz tube was heated at a rate of 10 °C.min^{-1} from 25 °C to 900 °C under 5% H_2/Ar gaseous flow (25 ml.min^{-1}). The outlet gas flow was passed through an ice bath to trap the water formed during reduction ($H_{2(g)}+NiO_{(s)}\rightarrow Ni^0_{(s)}+H_2O_{(g)}$) before

attaining the thermal conductivity detector (TCD). H_2 consumption was quantified by integrating the area of the TCD curve versus temperature and referring it to a calibration curve.

Thermogravimetric analysis (TGA), also expressed as differential thermogravimetric analyses (DTG), and coupled with differential thermal analysis (DTA), was performed on a TA SDT Q600 instrument working in horizontal mode. One of the two alumina crucibles was filled with about 25 mg of sample while the other (reference) crucible was kept empty. Both were located in the heating chamber and equipped with thermocouples to follow simultaneously weight and heat flow changes during heating, carried out in air flow (50 ml.min^{-1}) from room temperature to 900 °C with a ramping rate of 5 °C.min^{-1}. A capillary placed at the exit of the chamber and connected to a Fisons VG Thermolab Mass Spectrometer was also used to perform continuous mass spectrometry (MS) analysis of the exhaust gases.

Scanning Electron Microscopy (SEM) images were taken on a Hitachi SU-70 SEM-FEG microscope with an electron acceleration tension of 7 kV. After careful grinding, the samples were deposited on the analysis support and observed in mixed mode (70% of secondary electrons and 30% of retro-diffused signals). A JEOL-JEM 2010 electron microscope operating at 200 keV (LaB_6 gun) was used for High-Resolution transmission electron microscopy (HR-TEM) experiments. The observations were done on ultrathin sections of the samples prepared by mixing a few milligrams of the powder with an EPON 812 embedding resin in a beam capsule, heating the mixture at 60 °C for 48h to provoke polymerization, then cutting the polymerized blocks with a diamond knife. The obtained slices (50-70 nm in thickness) were deposited on copper grids covered with a carbon membrane layer. Average sizes of nickel particles, when visible, were estimated using the ImageJ software and taking at least 500 particles into consideration. Combined STEM-HAADF and EDX Mapping was performed on a JEOL-JEM 2020 microscope to visualize further the Ni distribution in ultra-thin sections (prepared as above) of a selected sample.

Raman spectra were collected on a KAISER (RXN1) optical system equipped with a charge-coupled detector (CCD), a laser with λ = 785 nm (energy of 1.58 eV) and a microscope with an X50 long working distance (W.D. = 8.0mm) lens. The operation conditions were as follows: 10 mW laser power, 4 cm^{-1} resolution, 10 s acquisition time and a total of 30 accumulations per spectrum.

2.3 Catalytic measurements

Catalytic performances were studied in a fixed bed reactor (Hastelloy X, I.D.=9 mm, L=30.5 cm) situated inside a micro activity reference catalytic reactor (MAR, PID Eng and Tech Spain). Typically, 50 mg of catalyst were loaded into the reactor and reduced *in situ* under 5 vol% H_2/Ar (30 ml.min^{-1}) at 800 °C for 2 h (heating rate 5 °C.min^{-1}). The temperature was then let to cool down to 650 °C, afterwards the reducing gas mixture was replaced by a flowing gas composed of an equimolar amount of CH_4 and CO_2 diluted in Ar (atomic ratio 5/5/90) and kept at atmospheric pressure and at a gas hourly space

velocity (GHSV) of 72 $L.g^{-1}.h^{-1}$. This protocol was chosen based on TPR data and on previous studies [19,20]. Catalytic performances were established from the gas composition at the exit of the reactor monitored with an INFICON micro GC along with a TCD and two parallel channels (Molecular sieve and Plot U). The data are reported after 0.5 h and 13 h of reaction (stability test) in terms of:

- reactants conversions, estimated from the equation "X conversion (%) = (C_{in} - C_{out}) / C_{in}", where C is the reactant (CH_4 or CO_2) and *in* and *out* represent the inlet and outlet concentrations of this gas, respectively,

- H_2/CO (mole ratio) = N_{H2} / N_{CO}", where N_{H2} and N_{CO} are the molar concentrations of the formed H_2 and CO products.

Carbon balance was systematically verified during the tests and was always above 98%.

3. Results

3.1 Characteristics of the parent MIL-53, activated MIL and impregnated Ni/MIL materials.

After synthesis in microwave conditions, the parent MIL-53 sample is characterized by a X-ray diffractogram (Fig. 2a) similar to that reported in the literature for a MIL-53 material synthesized with the same microwave procedure (MW) [42]. This validates the formation of the targeted MIL-53 framework that is known to display dynamic structure properties, implying pore size variations upon guest adsorption (so-called "breathing behavior") with an amplitude that depends on the size of the molecules adsorbed in the pores and on the strength of their interaction with the framework [43]. Such pores adaptation can explain the small differences observed between the PXRD pattern of the as-synthesized MIL-53 prepared here by MW and that commonly reported after synthesis under conventional heating [42], both methods inevitably leading to variations in the amounts of molecules (solvent and unreacted linkers) trapped within the pores due to different crystal formation rates.

After activation at 220 °C in air (to remove all adsorbates from the pores), the diffractogram changes to a completely different one (sample MIL, Fig. 2b), in accordance with the dynamic nature of the MIL-53 structure mentioned above. One can note however that the new PXRD pattern is not composed only of peaks belonging to the large pore form of MIL-53 (indicated by black triangles, typical of empty pores), but it also contains peaks related to the narrow pore form (indicated by black spheres) as well as reflections characteristic of an intermediate state between the open and closed forms (indicated by black diamonds). This multiphasic structural state is related to the thermal history of the sample as already described by others for MIL-53 [44] and can be taken as representative of the "activated form". As shown in Fig. 2d, all the peaks corresponding to this activated form are still present after Ni impregnation (Ni/MIL), even if slightly shifted and with distinct relative intensities for some of them. More importantly, new tiny peaks appear at unusual positions and they are visible both after drying in room atmosphere and at 200 °C (identified by stars, Fig. 2d and 2d', respectively). Such new reflections were to our knowledge never reported for MIL-53, strongly suggesting that nickel cations are

inserted within the pores where they provoke structural deformation by interacting with the framework as in the case of adsorbed organic guest molecules [45].

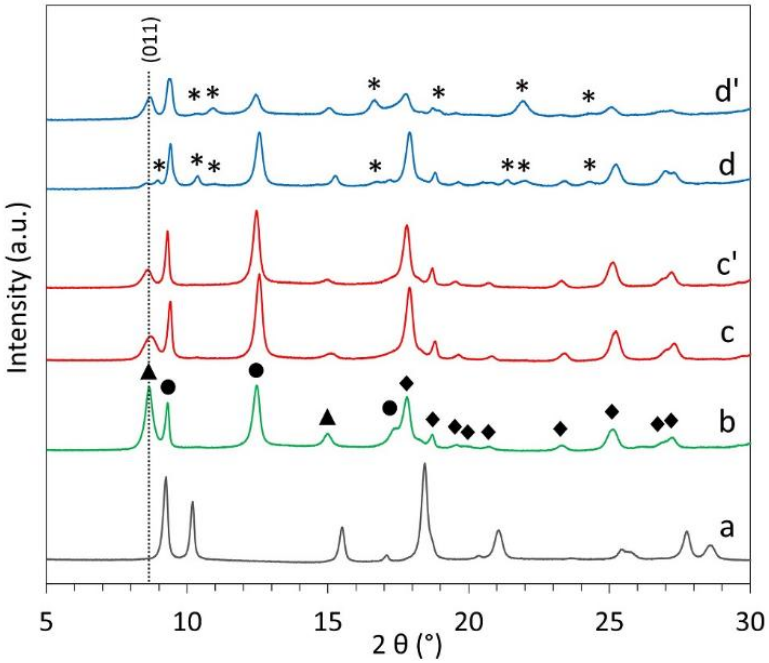

Figure 2. X-ray diffraction patterns of: (a) as synthesized MIL-53(Al), (b) activated MIL, (c) rehydrated MIL dried in room atmosphere or (c') at 200 °C, (d) impregnated Ni/MIL dried in room atmosphere or (d') at 200 °C. The dot vertical line emphasizes the position of the 011 reflection of the PXRD pattern corresponding to the MIL-53 large-pore phase. Triangles and spheres indicate the peak positions corresponding to the open and closed forms of the MIL-53 structure, respectively (as reported in [41]). Diamonds show unattributed reflections that may correspond to an intermediate state. Stars indicate peaks appearing after nickel impregnation.

In order to confirm the origin of these new reflections, a series of experiments was done with the aim to demonstrate that they appear only in the presence of Ni and do not simply come from different hydration states generating cell volumes and symmetry changes in response to the above-mentioned "breathing behavior". We prepared to this end a nickel free hydrated MIL sample to be compared to freshly impregnated Ni/MIL. This was done by immersing the freshly activated MIL powder into a volume of pure water equivalent to the one used for Ni impregnation. PXRD patterns were then taken, after submitting both rehydrated MIL and impregnated Ni/MIL to the same successive drying treatments consisting first in natural drying in room atmosphere (Fig. 2c and 2d) then in drying at 200 °C for 24h (Fig. 2c' and 2d'). Whatever the treatment, the additional tiny peaks (indicated by black stars) were present for Ni/MIL (Figures 2d and 2d') but not for MIL (Fig. 2c and 2c'). Together with the limited intensity of these peaks that fits well the limited Ni content in the samples, this systematic difference is

in line with a local framework distortion due to interaction with nickel cations occluded within the pores. Such distortion also agrees with the small shift to higher angle of the (011) reflection (at 2θ = 8.7°) of the large-pore phase pattern, which is particularly disturbed after nickel impregnation (Fig. 2d).

The presence of nickel within the pores is further supported by the strong decrease of the saturation volume of N_2 adsorbed at low relative pressure (P/P_0 = 0.2) in Ni/MIL (Fig. 3c) compared to both activated MIL (Fig. 3a) and rehydrated MIL (Fig. 3b), which corroborates a pore hindrance linked to the presence of Ni^{2+}. Accordingly, the microporous volume drops from 0.40 $cm^3.g^{-1}$ (activated MIL) to 0.09 $cm^3.g^{-1}$ upon nickel impregnation (Ni/MIL) and the BET specific surface simultaneously diminishes from 1130 $m^2.g^{-1}$ (MIL) to 300 $m^2.g^{-1}$ (Ni/MIL). By comparison, the pore volume is much less affected upon MIL rehydration (0.32 $cm^3.g^{-1}$), even if a small decrease is also noted, revealing some loss of structural integrity after water adsorption as well, probably at the origin of the PXRD peak broadening seen for both rehydrated (MIL) and impregnated (Ni/MIL) series of samples ((011) reflection at 2θ = 8.7° mainly, Fig. 2). Noteworthy, the N_2 adsorption-desorption isotherms of all materials (MIL, rehydrated MIL and Ni/MIL, Fig. 3a-c) also display a marked step at relative pressures above P/P_0 = 0.9 characteristic of a substantial intercrystalline meso-macro porosity occurring between aggregated nanocrystals.

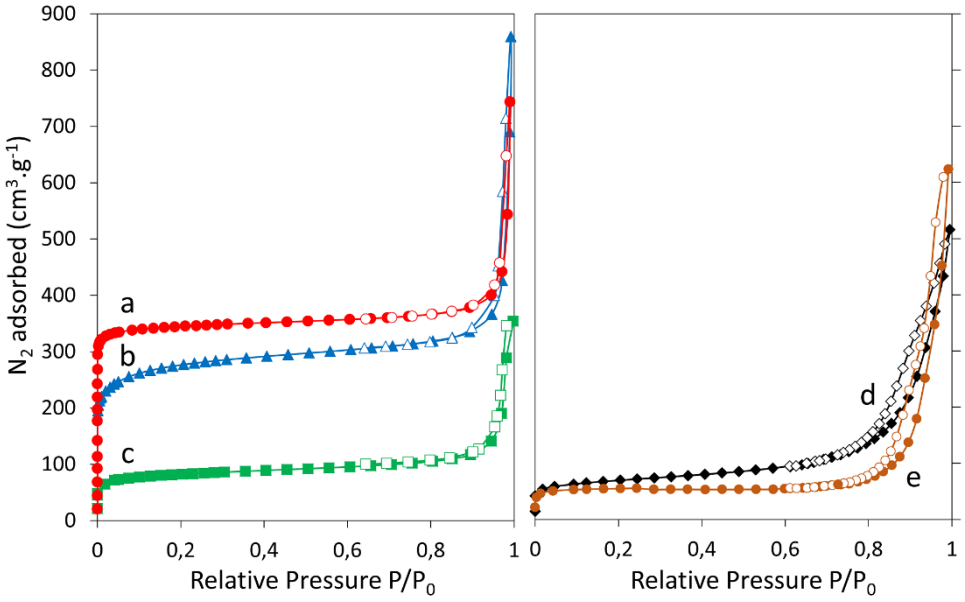

Figure 3. N_2 physisorption isotherms after degassing at 120 °C of: (a) freshly activated MIL (red spheres), (b) rehydrated MIL (blue triangles), (c) Ni/MIL (green squares), (d) $NiAl_{MIL}$ (black diamonds) and (e) Ni^0Al_{MIL} (brown spheres). Filled and empty symbols correspond to adsorption and desorption isotherms, respectively.

A last evidence of the intimate mixing between the nickel precursor species and the porous network in Ni/MIL is given by thermogravimetric analyses that show a weigh loss of about 15 % between 200 °C and 420 °C for this sample (Fig. 4Ac) but no loss in this temperature range for hydrated MIL (Fig. 4Ab).

As confirmed by the simultaneous MS detection of NO (mass 30) in the exhaust gas (Fig. 4B, bottom, blue curve), this weight loss corresponds to the thermal decomposition of nitrates introduced together with nickel during the impregnation step. Notably, the oxidizing nitrogen oxide species such as NO formed within the pores of Ni/MIL during heating induce a lowering by more than 60 °C of the temperature at which the carbonaceous (terephthalate) linkers degradation occurs (important weight loss between 400-550 °C, Fig. 4c, top) compared to both freshly activated and rehydrated MIL (process shifted to 500-650 °C for both of them, Fig. 4a and 4b). The DTG profiles (Fig. 4B, middle curves) reveal that the degradation takes place in two steps, as previously reported for the amino-teraphthalate MIL-125(Ti) [46]. The second step is accompanied by an evolution of CO_2 for both MIL and Ni/MIL and also of NO for Ni/MIL (see respective curves in Fig. 4B), and the process is strongly exothermic as seen from the DTA profiles (Fig. 4A, bottom curves). Hence, all data indicate that the linkers degradation is displaced towards a significantly lower temperature after nickel impregnation, giving the following scenario during heating of Ni/MIL: (1) the temperature increase up to 150 °C leads to the dehydration of the hexahydrate nickel nitrate used as nickel precursor according to the equation $Ni(NO_3)_2.6H_2O \rightarrow Ni(NO_3)_2 + 6H_2O$, the theoretical mass loss of 59% for this event being close to the 50% measured by TG; (2) this is followed between 200 and 400 °C by nitrates decomposition into NO_x (NO, NO_2, etc.) [47] with simultaneous formation of a NiO-based phase (for the sake of neutrality preservation); (3) then, strongly adsorbed NO_x oxidizers remaining within the pores in close proximity (or in contact) with the organic linkers promote their decomposition, decreasing the temperature at which it occurs [48].

In view of these TG profiles, we decided to set the calcination temperature of Ni/MIL during sample preparation (to form $NiAl_{MIL}$) at 500 °C, a temperature high enough to degrade the linkers but guaranteeing as well the development of the porosity and the large surface area of the pure mineral final phase. Indeed, it was recently reported that a temperature close to the onset of the parent MOF calcination temperature is optimal for the preparation of inorganic structures with preserved morphology and dimensions [38], which is important for preserving an intercrystalline porosity and large surface area in the obtained catalyst.

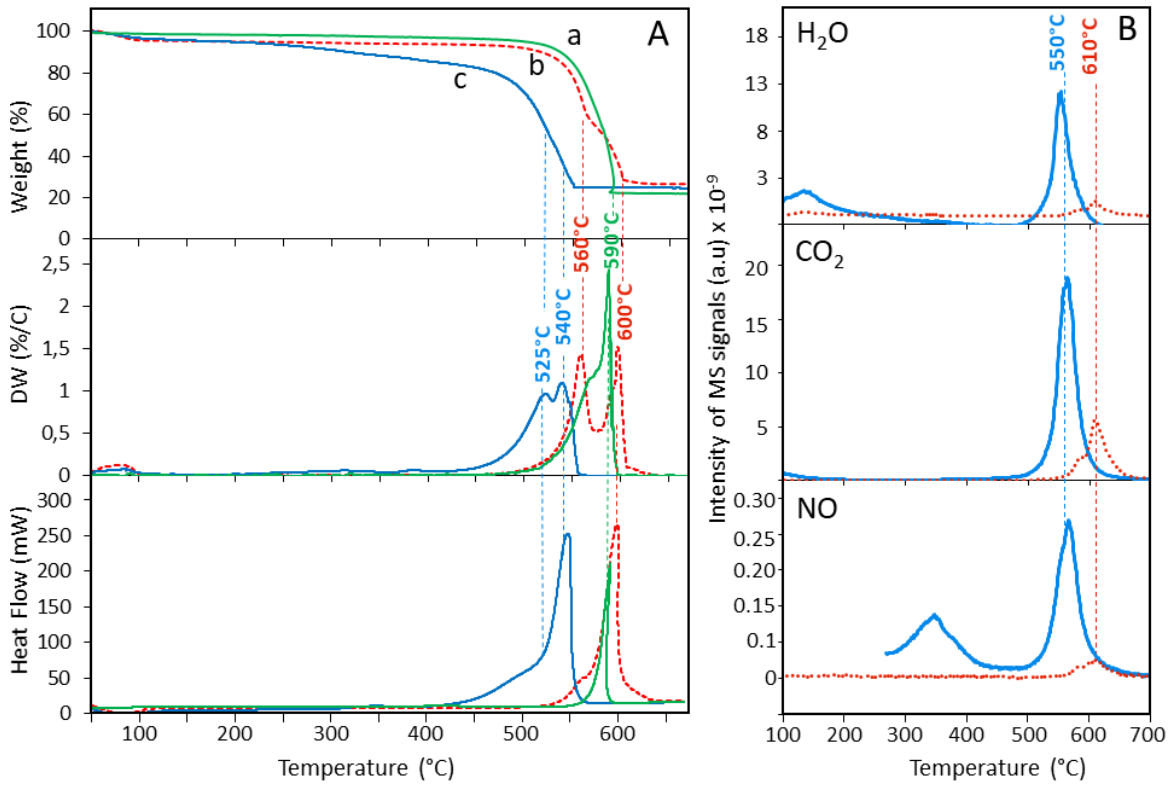

Figure 4. (A) TGA (top curves), DTG (middle curves) and DTA (bottom curves) profiles for samples: (a) freshly activated MIL (green lines), (b) rehydrated MIL (red dotted lines) and (c) impregnated Ni/MIL (blue lines). (B) Mass spectrometry profiles corresponding to the detection of H_2O (mass 18), NO (mass 30) and CO_2 (mass 44) for hydrated MIL (red dotted lines) and impregnated Ni/MIL (blue lines). The temperatures of peak maxima in Fig. 4B are slightly higher than in Fig. 4A due to the delay for the exhaust gases to reach the MS analysis chamber.

Table 1. Textural characteristics, reduction temperature and nickel content.

Sample names	Textural properties[a]			Reduction Temperature[b] (°C)	Ni content[c] (wt%)	Ni^0 nanoparticle size (nm)[d]		Ni^0 nanoparticle dispersion (%)[e]
	S.A. ($m^2.g^{-1}$)	V_{tot} ($cm^3.g^{-1}$)	Φ mean (nm)			reduced	spent	
MIL	1130	0.80	n.d					
$NiAl_{MIL}$	239	0.82	10	830	5.1 *(5.2)*			
Ni^0Al_{MIL}	200	1.02	16			6.8 (*5.3*)	7.5	19
Al_{MIL}	318	1.19	6.2					
$Ni@Al_{MIL}$	244	0.94	5.1	700/820	4.7 *(4.6)*			
$Ni^0@Al_{MIL}$	130	0.55	5.6			10.2 (*8.0*)	11.0	12
Al_{COM}	185	0.51	9.2					
$Ni@Al_{COM}$	168	0.47	9.9	630/800	5 *(5)*			
$Ni^0@Al_{COM}$	125	0.43	10.3			22 (*18*)	29	5.6

a: total surface area (S.A.), total pore volume (V_{tot}) and mean pore diameter (mean) calculated from the N_2 sorption isotherms.

b: temperature at the maximum of TPR peaks.

c: Ni contents determined from the amount of H_2 consumed during TPR taking into account that the theoretical amount is 860 µmol.g^{-1} for the reduction of 5wt% Ni^{2+}. In brackets: values determined by XRF.

d: mean size values calculated from the histograms obtained from representative TEM images of each samples. In brackets: values estimated from PXRD by applying the Scherrer equation considering the Ni^0 reflection at 2θ =51.9°. Note that the particle sizes could not be identified by PXRD after test because of the lack of sufficient amount of samples.

e: nanoparticle dispersion calculated from the formula $D = 6\times10^9\times (V_{Ni}/A_{Ni})\times(1/d)$ where d is the particle size (estimated from PXRD), V is the volume of Ni atom in the bulk metal and A is the area of the Ni surface atom [49][50].

3.2 Physicochemical properties of the calcined $NiAl_{MIL}$ and reference materials.

Fig. 5 and 6 show typical SEM and TEM micrographs of the parent (MIL) and impregnated then calcined ($NiAl_{MIL}$) materials. In both scanning (Fig. 5a) and transmission (Fig. 6a) modes, Ni/MIL appears as slightly elongated aggregated nanocristallites with uniform sizes of approximately 20 nm in length. Such morphology is coherent with the high intercrystalline volume identified above from N_2 physisorption. After calcination at 500 °C (sample $NiAl_{MIL}$, Fig. 5b and 6b), the size and shape of the nanograins are globally preserved although they tend to become thinner, forming fused ill-defined and more defective alumina flakes that are actually composed of several randomly interwoven nanosheets (inset in Fig. 6b). This is in line with the N_2 isotherm of this sample that displays features typical of layered mesoporous materials, namely (i) a progressive increase of the adsorbed N_2 volume, observed here at P/P_0 higher than 0.75 and (ii) a slit-type hysteresis spread over P/P_0 values, ranging here from 0.75 to 1 (Fig. 3d) and revealing a relatively polydisperse size distribution of large mesopores. The BET specific surface of 239 $m^2.g^{-1}$ is still high, even if much smaller than in the parent MIL material (Table 1) due to the organic linkers removal, and the microporous volume is close to that in Ni/MIL (Fig. 3d and 3c, respectively).

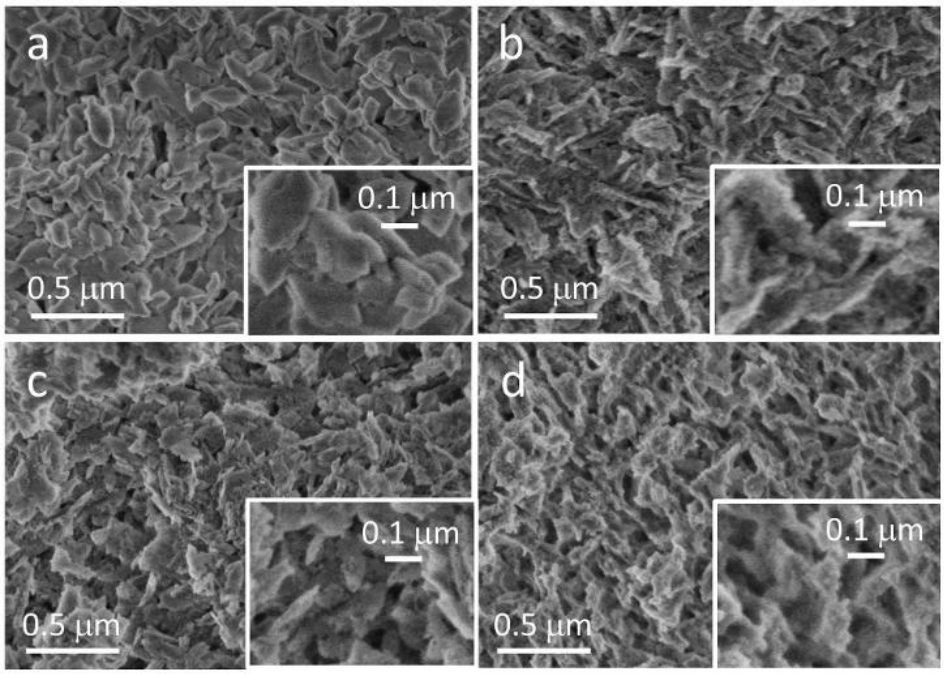

Figure 5. Representative SEM images of (a) MIL, (b) $NiAl_{MIL}$, (c) Al_{MIL} and (d) $Ni@Al_{MIL}$.

According to PXRD (Fig. 7a), these nanosheets structurally correspond to a cubic spinel $NiAl_2O_4$ phase with (400) and (440) planes giving main peaks at $2\theta = 45.0°$ and 65.6° [28,51,52]. They do not contain any peak attributable to crystalline NiO, confirming the intimate mixing between Ni and the oxide support, as also demonstrated by the temperature program reduction profile of NiAlMIL that displays only one peak centered at a high temperature of about 830°C (Table 1 and Fig. S1a) typical of

the formation of the spinel $NiAl_2O_4$ phase [53,54].The high and homogeneous Ni dispersion throughout the sample is also visible from STEM-HAADF and EDX elemental mappings that show the superimposed Ni and Al distributions on a representative $NiAl_{MIL}$ grain (Fig. 8).

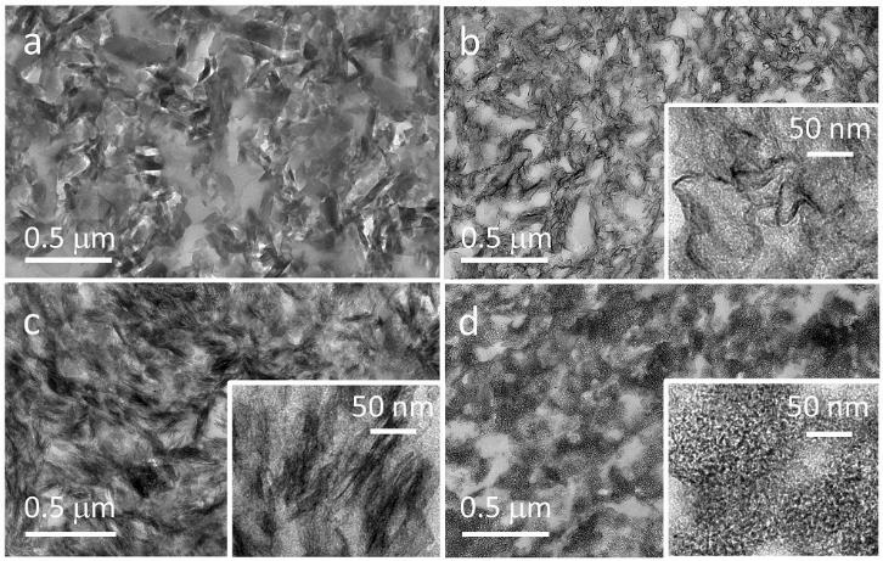

Figure 6. Representative HR-TEM images of (a) MIL, (b) $NiAl_{MIL}$, (c) Al_{MIL} and (d) $Ni@Al_{MIL}$.

In order to evaluate the impact on the material properties of the adopted preparation procedure (i.e. impregnating first the activated MIL with nickel then calcining it), a different order was applied by first calcining the activated MIL-53 (to obtain Al_{MIL}) then impregnating and calcining it at 500°C (to remove adsorbed nitrates and water molecules). This second sequence order, in which the impregnation is done on a preformed alumina support (here Al_{MIL}), resembles a conventional preparation route.

From PXRD, the structure of Al_{MIL} is typical of an amorphous alumina (Fig. 7b*). It changes after Ni impregnation and calcination (sample $Ni@Al_{MIL}$, Fig. 7b) to a crystalline phase very similar to that in $NiAl_{MIL}$ except for two reflections (2θ at 45.8° and 66.5°) that appear broadened and subtly shifted towards positions typical of γ-Al_2O_3 (2θ = 46.2° and 67.0°). This suggests a coexistence of both phases, as also supported by the TPR profile that contains two peaks, (i) a main one at high temperature (with maximum at T = 820 °C, Fig. S1b) indicative of some inclusion of nickel within the oxide matrix as in $NiAl_{MIL}$, and (ii) a smaller one centered at about 700 °C characteristic of nickel interacting less strongly with the alumina support (most probably nickel oxo-clusters on the external surface of the alumina grains). In term of morphology, the preformed alumina support appears as nanograins composed of both packed and interwoven nanosheets (sample Al_{MIL}, Fig. 5c and 6c) and this amorphous two-dimensional aspect is lost after nickel impregnation and calcination, turning to aggregates of tiny nanocrystals with ill-defined shapes (sample $Ni@Al_{MIL}$, Fig. 5d and 6d). Note that this final morphology significantly differs from the lamellar shape seen above for $NiAl_{MIL}$. Moreover, the grains appear assembled, forming a polycrystalline structure with polymodal porosity, in line with the three well defined steps observed in the N_2 adsorption isotherm of this sample (Fig. S2a), typical of the

coexistence of micro, meso and macropores. Therefore, the order of the “calcination / Ni^{2+} impregnation” sequence, which affected the temperature of degradation of the MIL organic linkers (TG/SM data, Fig. 4), also impacts the structure, texture and reducibility of the final material. To sum up, impregnation of the nickel cations within the activated MIL-53 to position them along the aluminum chains of the framework before the calcination step ($NiAl_{MIL}$) allows for a somewhat better dispersion (Table 1) and stabilization of nickel through their insertion into interwoven 2-dimensional alumina nanosheets. Notably, another advantage of this sequence order is to require only one calcination step during material preparation instead of two for conventionally impregnated $Ni@Al_{MIL}$.

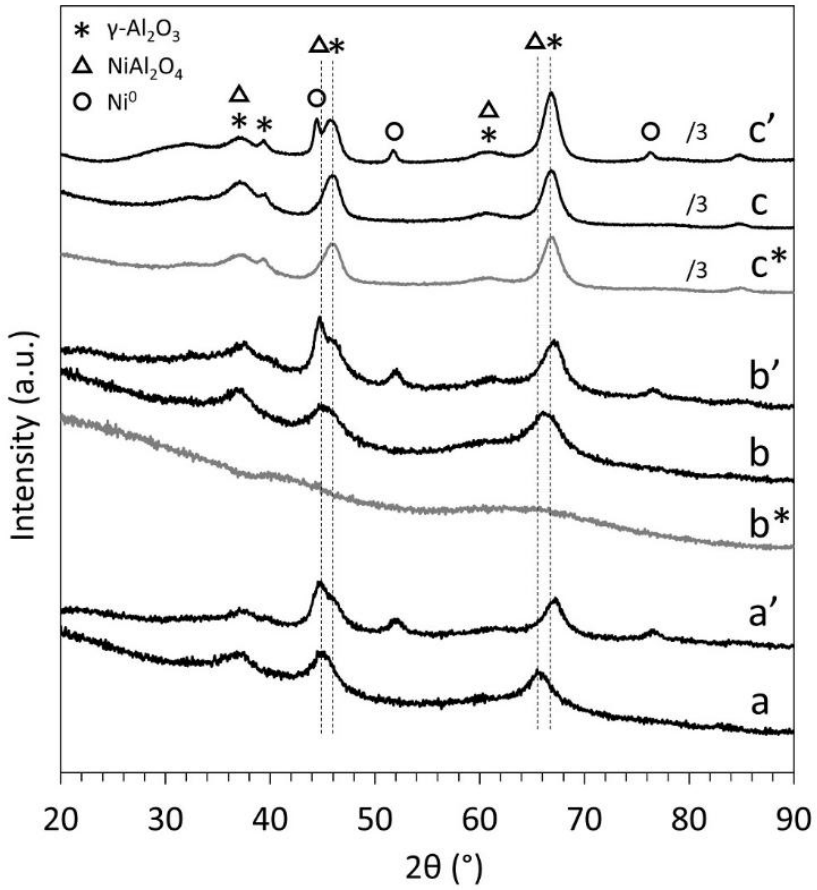

Figure 7. Diffractograms of the Ni containing samples: (a) $NiAl_{MIL}$, (a’) Ni^0Al_{MIL}, (b) $Ni@Al_{MIL}$, (b’) $Ni^0@Al_{MIL}$, (c) $Ni@Al_{COM}$, (c’) $Ni^0@Al_{COM}$. The diffractograms of the preformed alumina supports (light grey lines) are shown for comparison: (b*) Al_{MIL} and (c*) Al_{COM}. Intensities are divided by 3 in patterns c*, c and c’.

For the sake of comparison, a last material ($Ni@Al_{COM}$) was prepared by conventional nickel impregnation of a commercial γ-alumina (Al_{COM}) and tested as traditional reference catalyst. Both $Ni@Al_{COM}$ and its support Al_{COM} show four main diffraction peaks, which are typical of crystalline γ-Al_2O_3 (Fig. 7c* and 7c, respectively). No evidence of spinel phase can be observed on the diffractogram of $Ni@Al_{COM}$, although diffraction peaks corresponding to a small fraction of this phase might be masked

by those of the γ-Al_2O_3 phase. The TPR trace of this material displays two peaks, as for Ni@Al_{MIL}, but centered at lower temperatures than previously (630 °C and 800 °C, Fig. S1c), indicating a weaker Ni-support interaction than in both MOF-based samples, especially $NiAl_{MIL}$. Similarly to Ni@Al_{MIL}, a fraction of the nickel in Ni@Al_{COM} is probably existing in the material as amorphous NiO, as revealed by the TPR signal observed at relatively low temperature (T < 700°C). The significantly higher dispersion and stabilization of Ni in the latter sample can be explained as follows: the impregnation of nickel nitrate on the parent MIL-53 with especially high surface area enables the initial occlusion of the nickel precursors along the organic linkers and $[Al(OH)O]_n$ clusters decorating the pores, leading after the MOF calcination step (organic removal) to the formation of an Al_2O_3-$NiAl_2O_4$ phase in which nickel and aluminum cations are intimately mixed in a homogenous oxide phase. In contrast, impregnation of a preformed alumina (obtained by calcination of either MIL-53 or boehmite) then impregnation and calcination leads to a mixture of alumina, $NiAl_2O_3$ and NiO with an overall weaker interaction between nickel and the alumina matrix. Interestingly, the presence of nickel at the very first step of the preparation seems to direct the formation of the crystalline spinel $NiAl_2O_4$ phase during calcination (giving $NiAl_{MIL}$), while no spinel phase is formed when starting from pure MIL-53 (giving amorphous Al_{MIL}).

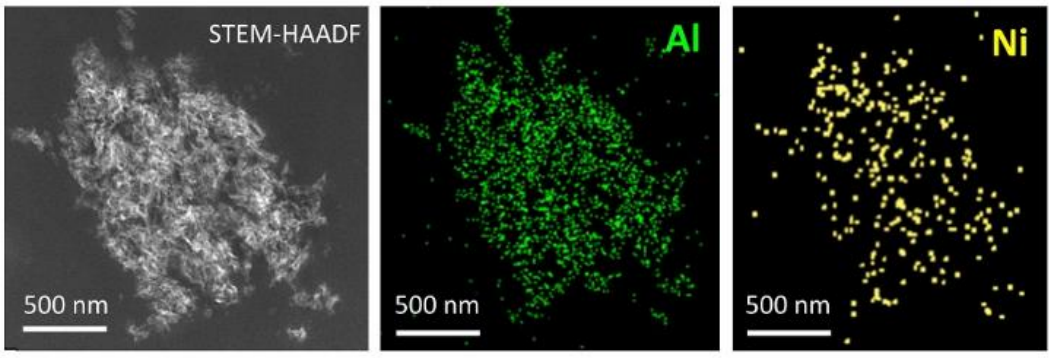

Figure 8. STEM-HAADF image of $NiAl_{MIL}$ (left) and EDX elemental mappings of the same area for Al (in green) and Ni (in yellow).

3.3 Characteristics of the reduced catalysts

Previous to catalytic tests, all the prepared nickel-alumina materials were treated under a flowing H_2 atmosphere to obtain reduced Ni^0, the active phase for DRM. The H_2 consumption during TPR was used to estimate the amount of reducible Ni^{2+} in all nickel containing samples, considering the consumption of one H_2 molecule per Ni^{2+} cation. For all samples, the Ni content is in accordance with that measured by X-fluorescence and close to the expected 5 wt% Ni, even if slightly lower, by less than 10%, for sample Ni^0@Al_{MIL} (Table 1).

The PXRD patterns of the samples reduced at 800 °C are shown in Fig. 7 and compared to those before reduction. The reduction of $NiAl_{MIL}$ to Ni^0Al_{MIL} leads to the formation of new diffraction peaks

assignable to the (111), (200) and (220) planes of crystalline Ni^0 (at 2θ = 44.5°, 51.9° and 76°, respectively, Fig. 7a'). Bands attributable to an alumina-based phase are still present but they are slightly shifted (compared to those before reduction) towards positions characteristic of pure γ-Al_2O_3 which attests of Ni extraction from the oxide matrix towards the pore surface. Application of the Scherrer equation to the Ni^0 reflection at 2θ = 51.9° leads to a mean Ni^0 nanoparticle size of 5.3 nm, slightly smaller than the value estimated by HR-TEM after measuring the sizes of at least 500 nanoparticles (Table 1). Considering the TEM image of Ni^0Al_{MIL} shown in Fig. 9a and the non-symmetrical shape of the histogram of particles sizes for this sample (Fig. 10), it can be assumed that this average size discrepancy comes from contrast issues making uneasy the detection of the smallest nanoparticles (from 2 to 4 nm) on the alumina grains, in spite of the good resolution of HR-TEM images. In this sample, all detected nickel nanoparticles are homogeneously distributed all over the support which still appears as interwoven alumina sheets (as in $NiAl_{MIL}$ before reduction). The preservation of the morphology after reduction is also attested by textural features, the N_2 physisorption isotherm of Ni^0Al_{MIL} still showing a slit-like hysteresis typical of a layered material composed of poorly organized interlayered pores (Fig. 3e). The amount of N_2 adsorbed at $P/P_0 > 0.8$ is however higher than that before reduction (Table 1), indicating the formation of additional large mesopores within the material. This increase of the total pore volume and mean pore size upon reduction is likely due to the exfoliation of the packed nanosheets through (i) the transformation of the $NiAl_2O_4$ spinel phase into γ-Al_2O_3 and (ii) the formation of the Ni^0 nanoparticles that may tend to further space apart the nanosheets one from another.

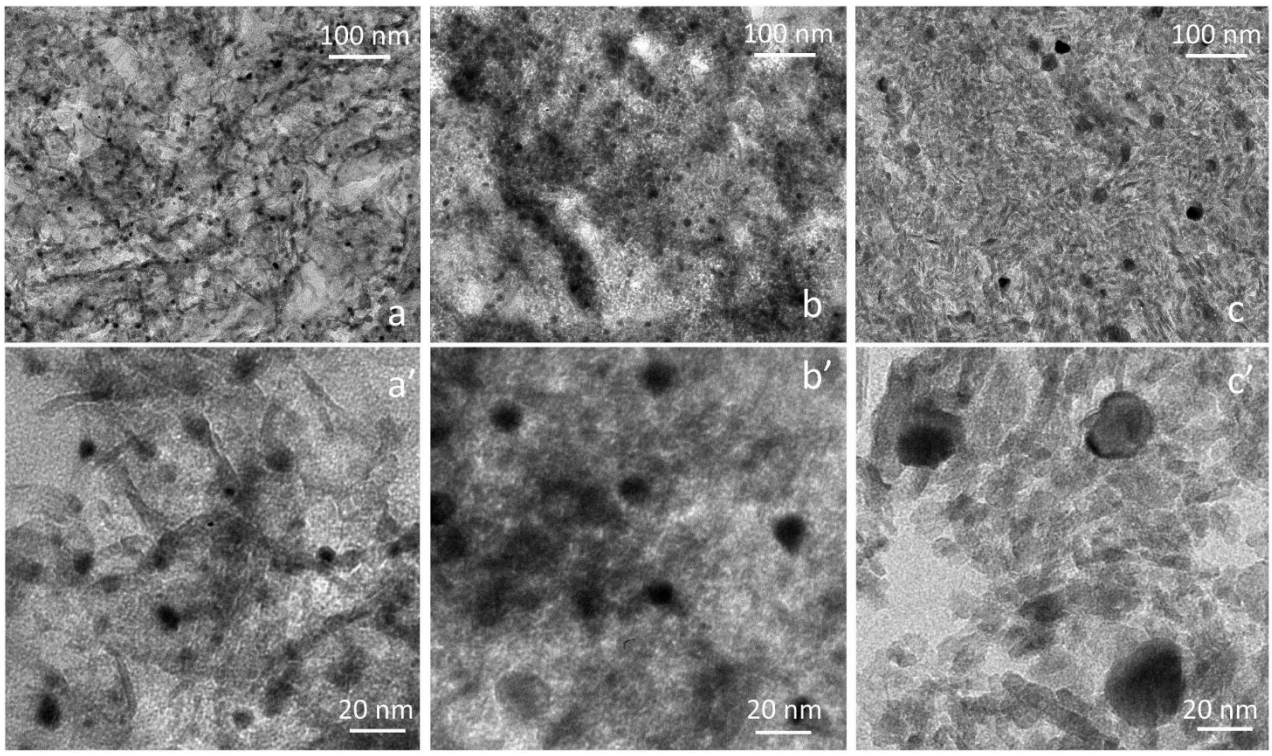

Figure 9. HR-TEM images of the reduced samples: (a and a') Ni^0Al_{MIL}, (b and b') $Ni^0@Al_{MIL}$, (c and c') Ni^0Al_{COM}.

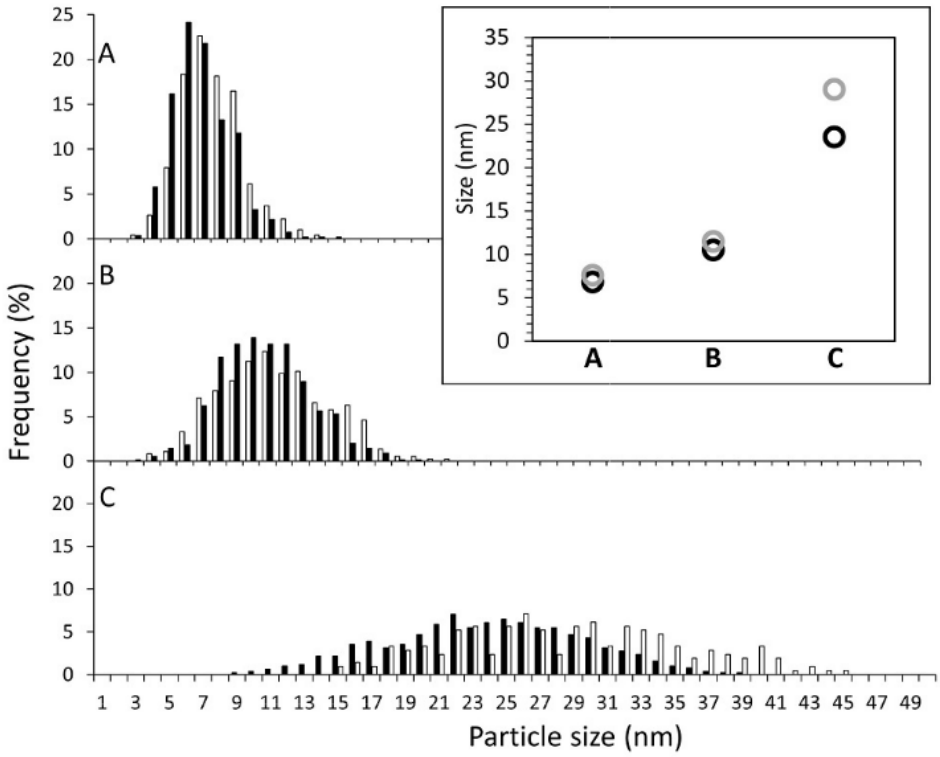

Figure 10. Histograms established from at least 500 Ni^0 nanoparticles in typical HR-TEM images of (A) Ni^0Al_{MIL}, (B) $Ni^0@Al_{MIL}$ and (C) $Ni^0@Al_{COM}$ before and after 13h of catalytic test (black and white bares, respectively). Related mean sizes are shown in (D) for the catalysts before (black circles) and after (grey circles) test.

The reduction of nickel impregnated on the two preformed alumina supports (Al_{MIL} and Al_{COM}) led similarly to the appearance of homogeneously dispersed Ni^0 nanoparticles (Fig. 9b and 9c, respectively), but the particles and their size distributions were systematically larger than on Ni^0Al_{MIL} (Table 1), especially in the case of Ni^0Al_{COM} (size = 22 nm) (Fig. 10). Hence, the homogeneous $NiAl_2O_4$-based spinel nanophase formation seen during the first steps of preparation of Ni^0Al_{MIL} and issued from initial nickel insertion within the pores of the MOF with high surface area before linker decomposition seems to play an important role towards metal stabilization with a positive effect that remains after partial extraction from the alumina matrix upon reduction.

3.4 Catalysis performances

Finally, the catalytic performances of Ni^0Al_{MIL} were tested in the reaction of dry reforming of methane and compared to those of $Ni^0@Al_{MIL}$ and $Ni@Al_{COM}$ (Fig. 11 and Table 2). After in situ reduction for 2 h at 800 °C to reduce nickel, each sample was cooled down to 650 °C and subjected to reaction for at least 13 h and for 100 h for Ni^0Al_{MIL}(stability test conditions). Fig. 11A and 11B show that the CO_2 and CH_4 conversions on both MOF-derived catalysts (Ni^0Al_{MIL} and $Ni^0@Al_{MIL}$) are high, close to thermodynamic equilibrium, and much higher (2 to 3 times) than those on $Ni^0@Al_{COM}$. Noteworthy, Ni^0Al_{MIL} is not only the most active catalyst but it is also very stable as its performance after the prolonged 100 h on stream remain nearly equal to that measured at the early stage of the reaction (Figure 11D). The selectivity to DRM on this sample is also remarkable, as attested by two features that indicate limited occurrence of side reactions: (i) the close CH_4 and CO_2 conversions that differ by only 7% (Fig. 11A and B) and (ii) the H_2:CO ratio very close to 1 (Fig. 11C). A rather good selectivity to DRM is also observed on $Ni^0@Al_{MIL}$ but with a H_2:CO ratio higher than 1 (Fig.11C) that suggests the occurrence of some CH_4 decomposition ($CH_4(g) \rightarrow C(s) + 2H_2(g)$). The formation of carbon deposits on the surface of this material is indeed confirmed by the 5 % weight loss detected at T = 600°C when the spent $Ni^0@Al_{MIL}$ is submitted to TGA analysis (Fig. 12A) as well as by the D and G bands visible by Raman spectroscopy (Fig. 12B) [27] and by the observation by scanning electron microscopy of carbon nanotubes on the catalyst surface (Fig. 13b and 13b'). Regarding the Raman signals, the two main bands (D and G) are typical of the doubly degenerated phonon mode of C atoms in the sp2 carbon networks with high degree of symmetry and of order (graphitic carbon, G-band, 1600 cm^{-1}) and of a disordered structural mode of carbon species (D-band, 1300 cm^{-1}). The intensity ratio between these two bands can be used as an indicator of the crystalline degree and of the presence of defects in the carbon species; the smaller the ratio (<1) the higher the structural order. Here, both $Ni@Al_{MIL}$ and $Ni@Al_{COM}$ have a ratio significantly higher than 1 (4.6 and 4.2 respectively) which indicates the disordered character of the carbon deposits, in line with the occurrence of carbon nanotubes observed on these samples by electron microscopy. Such deposits are similarly clearly identified on the spent $Ni^0@Al_{COM}$ catalysts, with a TGA weight loss (7 %) even higher (Fig. 12A) in spite of the low activity of this catalyst (low conversion level) and with D and G bands still clearly displayed on the Raman spectrograph (Fig. 12Bc). In contrast, such deposits are not detected on the most active Ni^0Al_{MIL} material, even after the 100 h test, neither by TGA (Figure 12A), nor by Raman spectroscopy (Fig. 12B) or electron microscopy (Fig. 13a and 13a'). Finally, the occurrence of side reactions on the reference $Ni^0@Al_{COM}$ material is confirmed by the products H_2:CO, which is initially below 1 and decreases with time (Fig. 11B), indicating some H_2 consumption through reverse water-gas shift (RWGS) reaction ($CO_2 + H_2 \rightarrow CO + H_2O$) and/or direct reduction of CO_2 ($CO_2 + 2H_2 \leftrightarrow C + 2H_2O$) that consumes a part of the produced H_2.

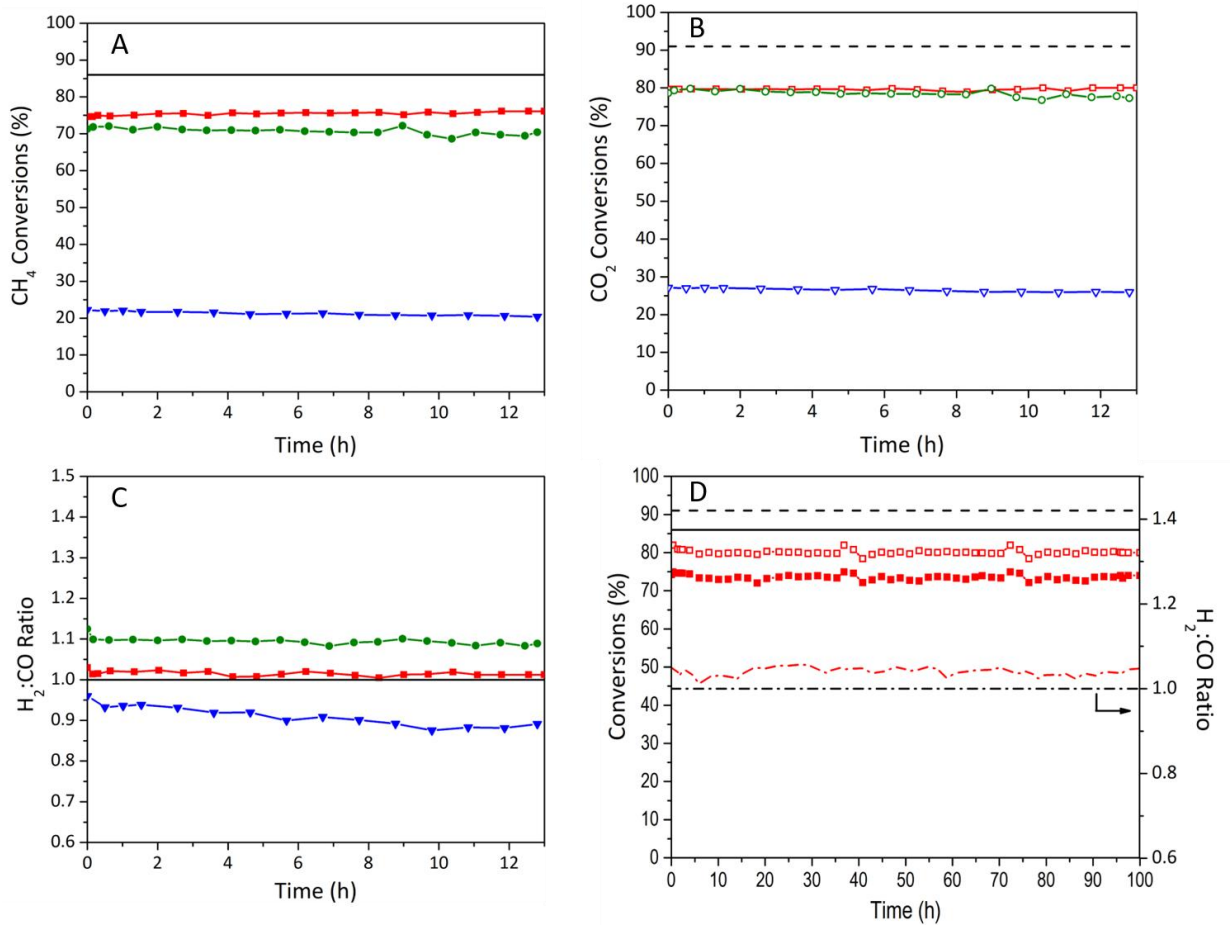

Figure 11. Comparison of the catalytic performances in DRM of the Ni^0Al_{MIL} (red squares), $Ni^0@Al_{MIL}$ (green spheres) and $Ni^0@Al_{COM}$ (blue triangles): (A) CH_4 conversion, (B) CO_2 conversion, (C) H_2:CO ratios measured during 13h of reaction and (D) CO_2 (filled squares) and CH_4 (empty squares) conversions as well as H_2:CO ratios (red dash-dotted line) measured during 100h of reaction for Ni^0Al_{MIL} (the black dash-dotted line represent H_2:CO = 1). Black continued and dashed lines are the calculated values at the thermodynamic equilibrium for the CH_4 and CO_2 conversions, respectively.

These results demonstrate the superior performances of the catalysts prepared from MIL-53, especially of Ni^0Al_{MIL} over $Ni^0@Al_{COM}$. The superiority of Ni^0Al_{MIL} in term of conversion is in line with the better Ni^0 dispersion in this sample (Fig. 13a and Table 1). It moreover reveals, together with the remarkable selectivity of Ni^0Al_{MIL} to DRM all along the run (higher than on $Ni^0@Al_{MIL}$ also prepared from MIL-53), a preservation of the active sites and hence a persistent strong nickel-support interaction even in the harsh conditions of reaction. This is seen by the high and comparable nickel dispersion both after reduction (Fig. 9a,a' and 10A) and after reaction (Fig. 10A and 13a). In contrast, a significant sintering takes place in $Ni@Al_{COM}$ in which the mean nickel particle size increases by about 30% after test (Table 1 and Fig. 10C,D). The formation in Ni^0Al_{MIL} of the stable spinel nickel aluminate phase, favored by the initial proximity between the nickel cations and the aluminum carboxylate clusters within the pore of MIL-53 during the calcination step, is believed to be at the origin of the stability of the dispersed Ni^0

nanoparticles. It could result from the presence of a remaining nickel aluminate spinel nanophase at the interface between the support and the metal nanoparticles after reduction that might insure a strong anchorage of the nanoparticles onto the resulting alumina support. One can also speculate that the layered texture of the material, which is remarkably well preserved during the 100h of reaction (Fig. 13a), contributes to the stability of the active phase as well by isolating and enhancing the occlusion of the nanoparticles, each of them being caught between two alumina sheets. This nanoparticle confinement effect may also explain the absence of carbon production on this sample. This explanation is in line with previous data showing that the occlusion of nickel nanoparticles within the mesopores of alumina supports prevent the catalysis of carbon nanotube formation, which occurs only from the nickel nanoparticles located on the external surface of the support [27].

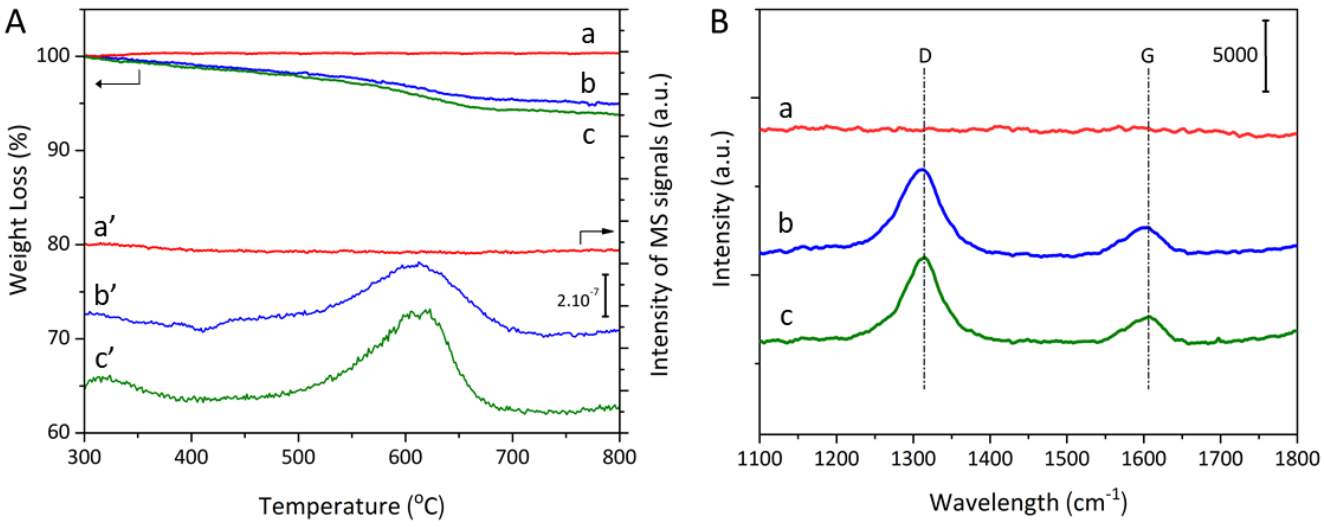

Figure 12. (A) TGA profiles (a, b, c at the top) associated to MS signals corresponding to CO_2 (a', b', c' at the bottom) and (B) Raman spectroscopy profiles of the spent catalysts (a, a') Ni^0Al_{MIL}, (b, b') $Ni^0@Al_{MIL}$ and (c, c') $Ni^0@Al_{COM}$.

Table 2. Catalytic test results obtained with Ni^0AlMIL and the comparative catalysts $Ni^0@Al_{MIL}$ and $Ni^0@Al_{COM}$.

Catalyst	Conversion (%)						Molar composition of main products			Coke content (%)	
	t=0.5h		t=13h		t=100h		t=0.5h	t=13h	t=100h	t=13h	t=100h
	XCH_4	XCO_2	XCH_4	XCO_2	XCH_4	XCO_2	H_2/CO	H_2/CO	H_2/CO		
$NiAl_{MIL}$	75	79	76	79	74	80	1.02	1.01	1.03	-	-
$Ni@Al_{MIL}$	71	79	70	77	n.p.	n.p.	1.12	1.09	n.p.	3	n.p.
$Ni@Al_{COM}$	22	27	20	26	n.p.	n.p.	0.93	0.89	n.p.	3	n.p.

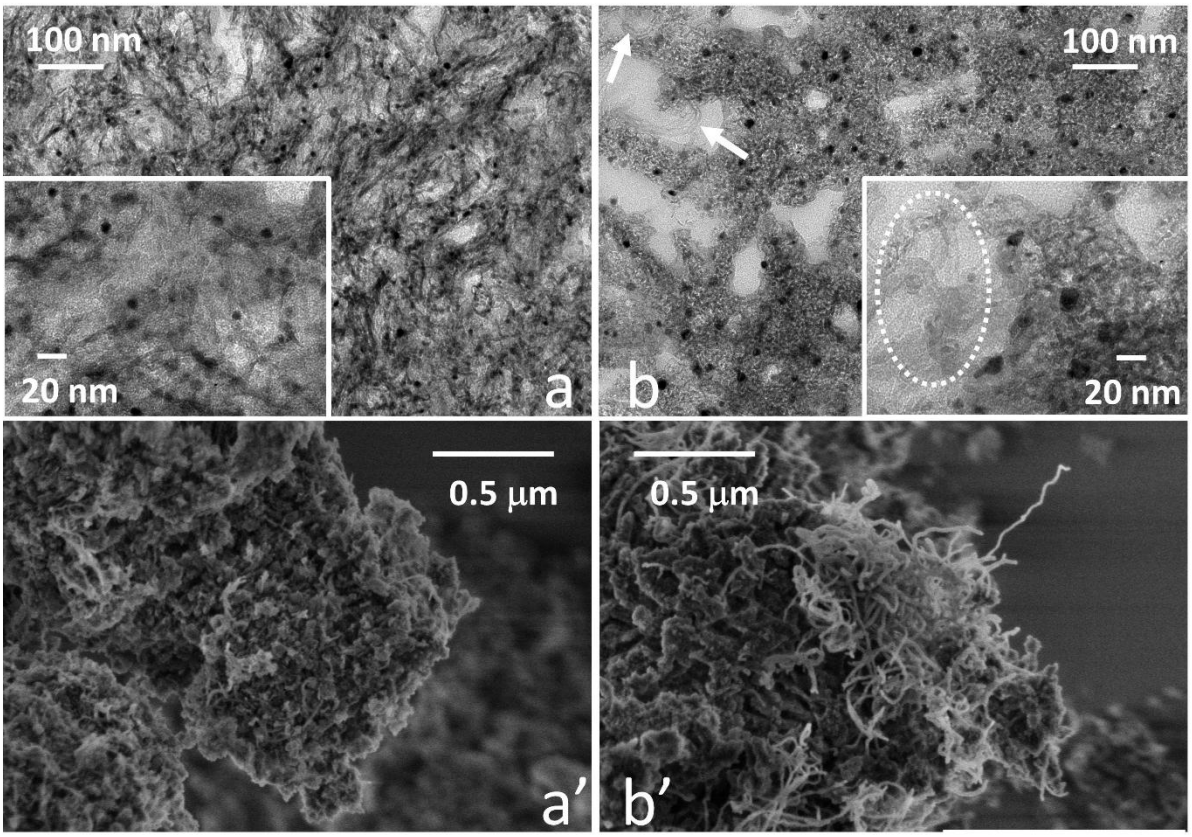

Figure 13. TEM (a,b) and SEM (a',b') images of spent $NiAl_{MIL}$ (a,a') and $Ni@Al_{MIL}$ (b,b'). The dashed oval and white arrows in (b) highlight the presence of carbon nanotubes.

It is worth adding that although the nickel nanoparticles reported here are not the smallest reported in the literature so far (the application of atomic layer deposition recently afforded nanoparticle size below 3 nm [55]), this study demonstrates the potential of MOFs as sacrificial hosts for preparing highly dispersed nickel nanoparticles whose size is below those prepared by employing other type of oxides as stable nickel cation hosts, such as alkaline earth metal substituted $MZr_{1-x}Ni_xO_3$-δ perovskites [56] or

the lanthanum zirconate pyrochlore La_2Zr_2-xNi_xO_7-δ [57]. Noteworthy, the use of MOF results in materials with a relatively high surface area (S. A. = 200 $m^2.g^{-1}$) compared to that obtained with other types of purely inorganic sacrificial nickel host cited above (S.A. < 20 $m^2.g^{-1}$), which can be seen as an additional benefit of this strategy in view catalysis applications.

4. Conclusion

In this work we demonstrate the benefit of using the aluminum carboxylate MIL-53 as a sacrificial nickel precursor host to prepare a dry methane reforming catalyst composed of nickel nanoparticles dispersed within a porous γ-Al_2O_3 lamellar phase. The higher surface area of this metal-organic framework compared to preformed porous alumina supports allows for a more efficient dispersion of the nickel precursors and, in turn, for a superior dispersion and uniformity of the nickel nanoparticles obtained after the MOF calcination and subsequent reduction steps. Consequently, the performances in terms of activity, selectivity and stability of this new catalyst for dry reforming of methane within the reaction conditions applied in this study are higher than those of comparative nickel@alumina catalysts prepared by conventional nickel impregnation of preformed alumina supports. Although the application of more severe reaction temperatures (e.g. temperatures higher than 800°C) and higher gas pressures would be necessary to evaluate the performances of this MIL-53-derived catalyst under more realistic DRM conditions, the results displayed in this report demonstrate that MOF can be considered as a promising hybrid alternative to the sacrificial inorganic and non-porous hosts (perovskite, hydrotalcites) used so far to stabilize nickel species towards the synthesis of catalysts based on nickel metal nanoparticles. In particular, employing MOFs as a sacrificial framework leads to materials with a higher surface area that those commonly encountered in the domain and whose interlamellar spaces may provide an additional stabilization to the confined nickel nanoparticles.

Considering the large variety of MOF compositions described so far, this approach is believed to be promising for the preparation of appealing catalysts applied for other types of greenhouse gas valorization reactions, such as methanation, as it will be soon demonstrated in a shortcoming contribution.

Supporting Information. TPR data, N_2 sorption isotherms of the samples Ni@Al_{MIL} and Ni@Al_{COM} as well as of the samples Al_{COM}, Ni@Al_{COM} and Ni^0@Al_{COM}. CH_4, CO_2 conversions and molar H_2/CO product ratio obtained after the test of dry reforming of methane during 100 h over in-situ reduced Ni^0Al_{MIL} catalyst.

*To whom correspondence should be addressed:
Julien.reboul@sorbonne-universite.fr

Acknowledgments. The authors sincerely acknowledge the ERANET EU-FP7 initiative, the national ANR (France) and CNRS-L (Lebanon) agencies for their financial support through the SOL-CARE (Energy-065) project (JC-ENERGY-2014 first call). The University of Balamand Research Council is also thanked for the BIRG 02/2016 contribution.

References:

[1] W.L. Luyben, Control of parallel dry methane and steam methane reforming processes for Fischer-Tropsch syngas, J. Process Control. 39 (2016) 77-87.

[2] L. E. I. Shi, G. Yang, K. A. I. Tao, Reforming with methane and new route of low-temperature methanol Synthesis, Acc. Chem. Res. 46 (2013) 2-11.

[3] Z. Navas-Anguita, P.L. Cruz, M. Martín-Gamboa, D. Iribarren, J. Dufour, Simulation and life cycle assessment of synthetic fuels produced via biogas dry reforming and Fischer-Tropsch synthesis, Fuel. 235 (2019) 1492-1500.

[4] Z. Hou, P. Chen, H. Fang, X. Zheng, T. Yashima, Production of synthesis gas via methane reforming with CO_2 on noble metals and small amount of noble- (Rh-) promoted Ni catalysts, Int. J. Hydrogen Energy. 31 (2006) 555-561.

[5] D. Pakhare, J. Spivey, A review of dry (CO_2) reforming of methane over noble metal catalysts, Chem. Soc. Rev. 43 (2014) 7813-7837.

[6] M. C. J. Bradford, M. A. Vannice, CO_2 Reforming of CH_4, Catal. Rev. 41 (1999) 1-42.

[7] J. R. Rostrup-Nielsen, J. B. Hansen, CO_2-reforming of methane over transition metals, J. Catal. 144 (1993) 38-49.

[8] Y. Gao, J. Jiang, Y. Meng, F. Yan, A. Aihemaiti, A review of recent developments in hydrogen production via biogas dry reforming, Energy Convers. Manag. 171 (2018) 133-155.

[9] B. Abdullah, N. A. Abd Ghani, D. V. N. Vo, Recent advances in dry reforming of methane over Ni-based catalysts, J. Clean. Prod. 162 (2017) 170-185.

[10] W. J. Jang, J. O. Shim, H. M. Kim, S. Y. Yoo, H. S. Roh, A review on dry reforming of methane in aspect of catalytic properties, Catal. Today. (2018) 0-1.

[11] J. H. Park, S. Yeo, I. Heo, T. S. Chang, Promotional effect of Al addition on the Co/ZrO_2 catalyst for dry reforming of CH_4, Appl. Catal. A Gen. 562 (2018) 120-131.

[12] L. Karam, N. El Hassan, Advantages of mesoporous silica based catalysts in methane reforming by CO_2 from kinetic perspective, J. Environ. Chem. Eng. 6 (2018) 4289-4297.

[13] J. Zhang, F. Li, Coke-resistant Ni at SiO_2 catalyst for dry reforming of methane, Appl. Catal. B Environ. 176–177 (2015) 513-521.

[14] T. J. Siang, S. Singh, O. Omoregbe, L. G. Bach, N. H. H. Phuc, D. V. N. Vo, Hydrogen production from CH_4 dry reforming over bimetallic $Ni–Co/Al_2O_3$ catalyst, J. Energy Inst. 91 (2018) 683–694.

[15] M. Németh, G. Sáfrán, A. Horváth, F. Somodi, Hindered methane decomposition on a coke-resistant $Ni-In/SiO_2$ dry reforming catalyst, Catal. Commun. 118 (2019) 56–59.

[16] J. Horlyck, C. Lawrey, E. C. Lovell, R. Amal, J. Scott, Elucidating the impact of Ni and Co loading on the selectivity of bimetallic NiCo catalysts for dry reforming of methane, Chem. Eng. J. 352 (2018) 572-580.

[17] G. P. Figueredo, R. L. B. A. Medeiros, H. P. Macedo, Â. A. S. de Oliveira, R. M. Braga, J. M. R. Mercury, M. A. F. Melo, D. M. A. Melo, A comparative study of dry reforming of methane over nickel catalysts supported on perovskite-type $LaAlO_3$ and commercial A-Al_2O_3, Int. J. Hydrogen Energy. 43 (2018) 11022–11037.

[18] J.H. Park, S. Yeo, T.S. Chang, Effect of supports on the performance of Co-based catalysts in methane dry reforming, J. CO_2 Util. 26 (2018) 465-475.

[19] N. El Hassan, M.N. Kaydouh, H. Geagea, H. El Zein, K. Jabbour, S. Casale, H. El Zakhem, P. Massiani, Low temperature dry reforming of methane on rhodium and cobalt based catalysts : Active phase stabilization by confinement in mesoporous SBA-15, Appl. Catal. A, Gen. 520 (2016) 114-121.

[20] L. Karam, S. Casale, H. El Zakhem, N. El Hassan, Tuning the properties of nickel nanoparticles inside SBA-15 mesopores for enhanced stability in methane reforming, J. CO_2 Util. 17 (2017) 119-124.

[21] M.N. Kaydouh, N. El Hassan, A. Davidson, S. Casale, H. El Zakhem, P. Massiani, Effect of the order of Ni and Ce addition in SBA-15 on the activity in dry reforming of methane, Comptes Rendus Chim. 18 (2015) 293-301.

[22] M. N. Kaydouh, N. El Hassan, A. Davidson, S. Casale, H. El Zakhem, P. Massiani, Highly active and stable Ni/SBA-15 catalysts prepared by a “two solvents” method for dry reforming of methane, Microporous Mesoporous Mater. 220 (2016) 99-109.

[23] K. Tao, L. Shi, Q. Ma, D. Wang, C. Zeng, C. Kong, M. Wu, L. Chen, S. Zhou, Y. Hu, N. Tsubaki, Methane reforming with carbon dioxide over mesoporous nickel-alumina composite catalyst, Chem. Eng. J. 221 (2013) 25-31.

[24] X. Lv, J. F. Chen, Y. Tan, Y. Zhang, A highly dispersed nickel supported catalyst for dry reforming of methane, Catal. Commun. 20 (2012) 6-11.

[25] K. Jabbour, N. El Hassan, A. Davidson, S. Casale, P. Massiani, Factors affecting the long-term stability of mesoporous nickel-based catalysts in combined steam and dry reforming of methane, Catal. Sci. Technol. 6 (2016) 4616-4631.

[26] S. M. Morris, P. F. Fulvio, M. Jaroniec, Ordered mesoporous alumina-supported metal oxides, J. Am. Chem. Soc. 130 (2008) 15210-15216.

[27] K. Jabbour, P. Massiani, A. Davidson, S. Casale, N. El Hassan, Ordered mesoporous “one-pot” synthesized Ni-Mg (Ca)-Al_2O_3 as effective and remarkably stable catalysts for combined steam and dry reforming of methane (CSDRM), Appl. Catal. B Environ. 201 (2017) 527-542.

[28] R. Benrabaa, A. Barama, H. Boukhlouf, J. Guerrero-Caballero, A. Rubbens, E. Bordes-Richard, A. Löfberg, R.N. Vannier, Physico-chemical properties and syngas production via dry reforming of methane over $NiAl_2O_4$ catalyst, Int. J. Hydrogen Energy. 42 (2017) 12989-12996.

[29] F. Rahbar Shamskar, M. Rezaei, F. Meshkani, The influence of Ni loading on the activity and coke formation of ultrasound-assisted co-precipitated Ni–Al_2O_3 nanocatalyst in dry reforming of methane, Int. J. Hydrogen Energy. 42 (2017) 4155-4164.

[30] L. Zhang, Q. Zhang, Y. Liu, Y. Zhang, Dry reforming of methane over Ni/MgO-Al_2O_3 catalysts prepared by two-step hydrothermal method, Appl. Surf. Sci. 389 (2016) 25-33.

[31] Z. Hou, T. Yashima, Meso-porous Ni/Mg/Al catalysts for methane reforming with CO_2, Appl. Catal. A Gen. 261 (2004) 205-209.

[32] K. Takehira, T. Shishido, P. Wang, T. Kosaka, K. Takaki, Autothermal reforming of CH_4 over supported Ni catalysts prepared from Mg-Al hydrotalcite-like anionic clay, J. Catal. 221 (2004) 43-54.

[33] L. He, H. Berntsen, E. Ochoa-Fernández, J. C. Walmsley, E. A. Blekkan, D. Chen, Co-Ni catalysts derived from hydrotalcite-like materials for hydrogen production by ethanol steam reforming, Top. Catal. 52 (2009) 206-217.

[34] N. Stock, S. Biswas, Synthesis of Metal-Organic Frameworks (MOFs): Routes to Various MOF topologies, morphologies, and composites, Chem. Rev. 112 (2011) 933-969.

[35] D. Yuan, J. Chen, S. Tan, N. Xia, Y. Liu, Worm-like mesoporous carbon synthesized from metal-organic coordination polymers for supercapacitors, Electrochem. Commun. 11 (2009) 1191-1194.

[36] X. Yan, N. Lu, B. Fan, J. Bao, D. Pan, M. Wang, R. Li, Synthesis of mesoporous and tetragonal zirconia with inherited morphology from metal-organic frameworks, CrystEngComm. 17 (2015) 6426-6433.

[37] H. Zhao, H. Song, L. Xu, L. Chou, Isobutane dehydrogenation over the mesoporous Cr_2O_3/Al_2O_3 catalysts synthesized from a metal-organic framework MIL-101, Appl. Catal. A Gen. 456 (2013) 188-196.

[38] Y. Lü, W. Zhan, Y. He, Y. Wang, X. Kong, Q. Kuang, Z. Xie, L. Zheng, MOF-templated synthesis of porous Co_3O_4 concave nanocubes with high specific surface area and their gas sensing properties, ACS Appl. Mater. Interfaces. 6 (2014) 4186-4195.

[39] Y. Liu, S. Liu, Z. Yue, Mesoporous alumina nanosheets and nanorolls derived from topologically identical Al-based MOFs, RSC Adv. 5 (2015) 31742-31745.

[40] Zehua Li, Yi-nan Wu,Jie Li, Yiming Zhang,Xin Zou, and Fengting Li The Metal–Organic Framework MIL-53(Al) Constructed from Multiple Metal Sources:Alumina, Aluminum Hydroxide, and Boehmite, Chem. Eur.J .2015, 21,6913-6920.

[41] Lo S.-H., Senthil Raja, D., Chen C.-W., Kang Y.-H., Chen J.-J., Lin C.-H. Waste polyethylene terephthalate (PET) materials as sustainable precursors for the synthesis of nanoporous MOFs, MIL-47, MIL-53(Cr, Al, Ga) and MIL-101(Cr) Dalton Trans., 45 (2016) 9565-9573.

[42] V.I. Isaeva, A.L. Tarasov, V. V. Chernyshev, L.M. Kustov, Control of morphology and size of microporous framework MIL-53(Al) crystals by synthesis procedure, Mendeleev Commun. 25 (2015) 466-467.

[43] T. Loiseau, C. Serre, C. Huguenard, G. Fink, F. Taulelle, M. Henry, T. Bataille, G. Férey, A rationale for the large breathing of the porous aluminum terephthalate (MIL-53) upon hydration, Chem.-A Eur. J. 10 (2004) 1373-1382.

[44] J. O. Hsieh, K. J. Balkus, J. P. Ferraris, I. H. Musselman, MIL-53 frameworks in mixed-matrix membranes. Microporous Mesoporous Mater. 196 (2014) 165-174.

[45] P. Horcajada, C. Serre, G. Maurin, N. A. Ramsahye, F. Balas, M. Vallet-Regí, M. Sebban, F. Taulelle, G. Férey, Flexible Porous Metal-Organic Frameworks for a Controlled Drug Delivery, J. Am. Chem. Soc. 130 (2008) 6774-6780.

[46] S. Hu, M. Liu, K. Li, C. Song, G. Zhang, X. Guo, Surfactant-assisted synthesis of hierarchical NH2-MIL-125 for the removal of organic dyes, RSC Adv. 7 (2017) 581-587.

[47] S. Yuvaraj, F. Y. Lin, T. H. Chang, C. T. Yeh, Thermal decomposition of metal nitrates in air and hydrogen environments, J. Phys. Chem. B. 107 (2003) 1044-1047.

[48] S. M. Pourmortazavi, S. G. Hosseini, M. Rahimi-Nasrabadi, S.S. Hajimirsadeghi, H. Momenian, Effect of nitrate content on thermal decomposition of nitrocellulose, J. Hazard. Mater. 162 (2009) 1141-1144.

[49] I. Luisetto, S. Tuti, C. Romano, M. Boaro, E. Di Bartolomeo, J. Kopula Kesavan, S. Murugesan S. Kumar, K. Selvakumar, Dry reforming of methane over Ni supported on doped CeO_2: New insight on the role of dopants for CO_2 activation, J.CO_2 Util. 30 (2019) 63-78.

[50] L. Pino, C. Italiano, A. Vita, M. Laganà, V. Recupero, $Ce_{0.70}La_{0.20}Ni_{0.10}O_{2-\delta}$ catalyst for methane dry reforming: Influence of reduction temperature on the catalytic activity and stability, Appl. Catal., B, 218 (2017) 779-792.

[51] L. Zhou, L. Li, N. Wei, J. Li, J. M. Basset, Effect of $NiAl_2O_4$ formation on Ni/Al_2O_3 stability during dry reforming of methane, ChemCatChem. 7 (2015) 2508–2516.

[52] H. Drobná, M. Kout, A. Sołtysek, V. M. González-Delacruz, A. Caballero, L. Čapek, Analysis of Ni species formed on zeolites, mesoporous silica and alumina supports and their catalytic behavior in the dry reforming of methane, React. Kinet. Mech. Catal. 121 (2017) 255-274.

[53] A. R. J. M. Mattos, S. H. Probst, J.C. Afonso, M. Schmal, Hydrogenation of 2-ethyl-hexen-2-al on Ni/Al_2O_3 catalysts, J. Braz. Chem. Soc. 15 (2004) 760-766.

[54] M. Shah, S. Das, A. K. Nayak, P. Mondal, A. Bordoloi, Smart designing of metal-support interface for imperishable dry reforming catalyst, Appl. Catal. A Gen. 556 (2018) 137-154.

[55] L. Li, Z. Shang, Z. Xiao, L. Wang, X. Liang, G. Liu, Steam reforming of n-dodecane over mesoporous alumina supported nickel catalysts: Effects of metal-support interaction on nickel catalysts, Int. J. Hydrog. Energy, 44 (2019) 6965-6977.

[56] S. Dama, S. R. Ghodke, R. Bobade, H. R. Gurav, S. Chilukuri, Active and durable alkaline earth metal substituted perovskite catalysts for dry reforming of methane, Appl. Catal., B, 224 (2018) 146-158.

[57] E. le Saché, L. Pastor-Pérez, D. Watson, A. Sepúlveda-Escribano, T.R. Reina, Ni stabilised on inorganic complex structures: superior catalysts for chemical CO_2 recycling via dry reforming of methane, Appl. Catal., B, 236 (2018) 458-465.